

ASSESSING THE QUALITY OF THE NEAR REAL-TIME REGIONAL VTEC MAPS PRODUCED BY LA PLATA UNIVERSITY IN ABSOLUTE GNSS POSITIONING OVER BRAZIL

Avaliação da qualidade dos mapas de VTEC regionais em quase tempo real produzidos pela Universidade de La Plata no posicionamento GNSS absoluto no Brasil

Thiago Amaral Pereira¹ – ORCID: 0000-0002-9759-5041
Wagner Carrupt Machado² – ORCID: 0000-0003-3112-7808
Haroldo Antonio Marques³ – ORCID: 0000-0001-9535-8723

¹ Universidade Federal de Uberlândia, Instituto de Geografia, Monte Carmelo – MG, Brasil.
E-mail: thiagoamaralpiri@gmail.com

² Universidade Federal de Uberlândia, Faculdade de Engenharia Civil, Monte Carmelo – MG, Brasil.
E-mail: wcarrupt@gmail.com

³ Instituto Militar de Engenharia - IME, Seção de Engenharia Cartográfica, Rio de Janeiro - RJ, Brasil.
E-mail: haroldoh2o@gmail.com

Received in 13th November 2020.

Accepted in 15th October 2021.

Abstract:

At the end of 2018, the Laboratorio de Meteorología Espacial, Atmósfera Terrestre, Geodesia, Geodinámica, Diseño de Instrumental y Astrometría, from La Plata University, started providing near real-time Regional Ionosphere Maps (MAGN) with high spatial and temporal resolutions and low latency. In this paper, we show a performance evaluation of these new ionosphere maps in space of positioning during the first year (2019) of available data. The assessment was carried out through absolute GNSS positioning using the in-house RT-PPP software. Data from five stations in Brazil, distributed in different geomagnetic latitudes, were processed. The performance of the MAGN was evaluated comparing the coordinates estimated using MAGN maps and the Global Ionosphere Maps (GIM) from CODE, both concerning the PPP ionosphere-free combination solution. Although it has been found that, in general, the MAGN and CODE solutions are compatible, the former provided better positioning result (8.5%) in the altimetric (up) component. However, when an atypical behavior in the MAGN solution at the end of the year 2019 as well as days of incomplete maps were removed from the analysis, the solution with MAGN becomes slightly better than CODE, providing an improvement of 8.6% in the up component.

Keywords: GNSS positioning; Regional Ionosphere Maps; Global Ionosphere Maps; MAGGIA.

How to cite this article: PEREIRA, T.A.; MACHADO, W.C.; MARQUES, H.A. Assessing the quality of the near real-time regional VTEC maps produced by La Plata University in absolute GNSS positioning over Brazil. *Bulletin of Geodetic Sciences*. 27(4): e2021028, 2021.



This content is licensed under a Creative Commons Attribution 4.0 International License.

1. Introduction

When performing GNSS positioning using single-frequency data, the user can estimate the ionosphere together with other parameters, apply corrections from the ionosphere mathematical models or compute ionosphere corrections from Vertical Total Electron Content (VTEC) maps. Although various ionospheric mathematical models can be used, most of them are capable of correct about 50% of the ionospheric delay. The most popular ionosphere model is the Klobuchar, whose coefficients are transmitted through the GPS broadcast navigation message (Klobuchar 1987). Galileo satellites also transmit information to be used in the NeQuickG model (Radicella 2009; European Commission 2016). Setti Júnior et al. (2019) investigated the accuracy of multi-GNSS (GPS and Galileo) single-frequency positioning using, respectively, the Klobuchar and NeQuick models and taking into account data from years 2013 to 2018. When comparing with positioning without ionosphere correction, the NeQuick model provided accuracy improvements of 31% and 55%, respectively, for low and high solar activity periods, while for the Klobuchar such improvements reach respectively 16% and 50%.

Another way to correct the first-order ionospheric delay is using the ionosphere maps that are estimated from continuous GNSS networks tracking dual-frequency data. An example is the Global Ionosphere Map (GIM) supplied by the International GNSS Service (IGS), which provides values of VTEC and Differential Code Biases (DCB) from data collected by the IGS network. Such maps are available free of charge in IONosphere Map EXchange format (IONEX) (Schaer, Gurtner and Feltens 1998) and allow the user to improve the positioning solution.

Armendaris et. al, 2009 showed the accuracy improvement of the Single Point Positioning (SPP) using ionospheric corrections from GIM and considering GPS data from Porto Alegre (POAL) station, which belongs to the Brazilian Network for Continuous Monitoring of the GNSS Systems (RBMC). The results reached 77% of improvement in altimetry and 44% in planimetry when compared with SPP without ionosphere correction.

It is also important to mention the regional ionosphere model for Brazil, called GIB (Brazilian Ionospheric Grid). Experiments considering two days in January of 2014 (high solar activity period) showed an average improvement in the SPP accuracy of 77.4%, 44.7% and 74.6%, respectively, for the X, Y and Z coordinates in contrast with a solution without ionospheric correction (Aguiar and Kozelinski 2015). We can also cite the extinct Regional Ionosphere Maps (RIM) produced by La Plata University, Argentina, called La Plata Ionospheric Model (LPIM), which were evaluated in the absolute positioning for Brazilian stations during the year 2013 and showed a maximum annual improvement ranging from 22% to 37% compared to the solution applying the Center for Orbit Determination of Europe (CODE) GIM (Rocha, Marques and Monico 2015).

A new possibility of ionospheric correction available for Latin America is the near real-time Regional Ionosphere Maps produced by the Laboratorio de Meteorología espacial, Atmósfera terrestre, Geodesia, Geodinámica, diseño de Instrumental y Astrometría (MAGGIA) of La Plata University, hereafter referred to as MAGN-RIM. Such maps have been available from the end of 2018 and present better spatial and temporal resolutions, as well as lower latency than the GIM (Mendoza, Meza and Aragón Paz 2019a).

In this paper, we evaluate the performance of the MAGN maps in the absolute GPS positioning. We processed data from five GNSS stations well distributed over the Brazilian region and the MAGN-RIM solution performance was analyzed by comparing with the positions obtained using the CODE-GIM.

2. An overview of ionosphere maps determination

The ionosphere maps could be described as a set of regular grids with VTEC values, given in TEC units (10^{16} el/m²), spaced at pre-established time intervals. Additionally, they can provide satellite and receiver DCBs.

There is a complex infrastructure behind the production of near real-time ionosphere maps, involving the network dual-frequency GNSS data tracking, the real-time communication protocols, mathematical models and data processing (Komjathy 1997; Schaer 1999; Camargo 1999; Mendoza, et al. 2019b; Wang, et al. 2021). In Latin America, the SIRGAS-CON and Brazilian RBMC are examples of GNSS networks providing real-time data.

One of the most employed solutions to generate ionosphere maps applies the concept of the ionospheric thin-shell, where the Slant TEC (STEC) is considered to be fully contained at the Ionospheric Piercing Points (IPP). Instead of estimating the STEC, a mapping function is used to map TEC to the vertical direction (Komjathy 1997; Schaer 1999; Camargo 1999).

Classical post-processed ionosphere map solutions are provided with a certain time delay, varying from 1 to 11 days. However, with the advent of Networked Transport of RTCM via Internet Protocol (NTRIP), near real-time solutions can be implemented (Aguiar and Kozelinski 2015; Mendoza, Meza and Aragón Paz 2019a).

To compute the ionospheric correction from maps, the user must perform both spatial and temporal interpolations considering the VTECs along the grid vertices, as well as the IPP and the desired epoch (Schaer, Gurtner and Feltens 1998). Besides that, it is necessary to apply a mapping function to the interpolated VTEC to obtain the STEC. The standard geometric mapping function is given by (Hofmann-Wellenhof, Lichtenegger and Wasle 2008):

$$STEC = \frac{VTEC}{\cos(z')} \quad (1)$$

where z' represents the zenith angle at the IPP and can be computed by (Hofmann-Wellenhof, Lichtenegger and Wasle 2008):

$$\sin(z') = \frac{Re}{Re + hm} \sin(z) \quad (2)$$

where Re is the Earth's mean radius ($\cong 6371$ km); z is the zenith angle at the observing site and hm is the ionospheric layer mean height, generally, adopted as 450 km.

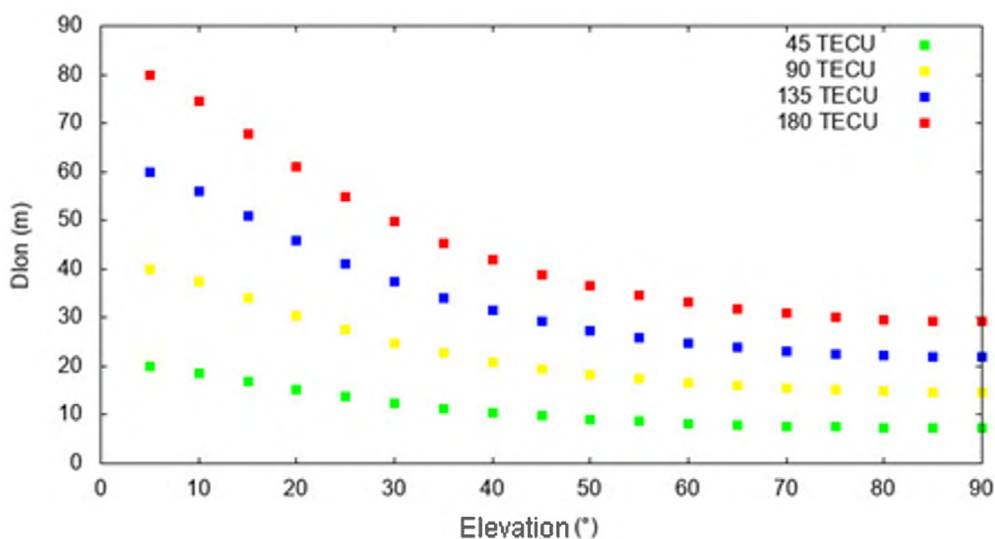
Thus, the ionospheric delay to be accounted for pseudorange and carrier-phase is computed respectively by:

$$Ion_{PD,i} = \frac{40.3STEC}{f_i^2} \quad (3)$$

$$Ion_{\phi,i} = -\frac{40.3STEC}{f_i^2} \quad (4)$$

where f_i is the i^{th} carrier frequency.

Figure 1 shows the relation between the ionospheric delay (Dion) and the elevation angle. Some VTEC values (45, 90, 135, and 180 TECU) were mapped to STEC using the standard geometric mapping function. We can observe from Figure 1 that the higher the VTEC value, the greater the amplitude of the ionospheric delay, mainly for low elevation angles.



Source: the authors.

Figure 1: Relationship between ionospheric delay and elevation angle.

2.1 Characteristics of Regional and Global Ionosphere Maps

Global Ionosphere Maps contain VTEC grids with a longitudinal range of 360° (with an interval from -180° to 180° and a spacing of 5°), while the latitudinal amplitude is 175° (from -87.5° to 87.5° with an interval of 2.5°). It is important to notice that the estimation of the GIM requires the GNSS data from a network with global coverage.

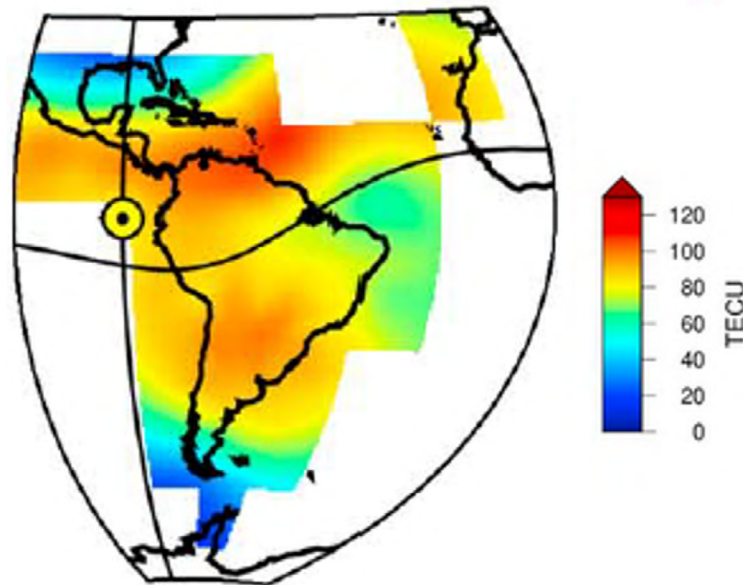
IGS provides rapid and final versions of GIM, with 24 h and 11 days of latency, respectively. The GIM produced by IGS is available in IONEX format with temporal resolution of two hours, where the final maps are traditionally obtained from the combination of four Ionosphere Associated Analysis Centers (IAAC): CODE, European Space Agency (ESA), Nasa Jet Propulsion Laboratory (JPL), and the Polytechnic University of Catalonia (UPC). Additionally, during the beginning of 2016, the Natural Resources of Canada (NRCAN) start delivering GIM to IGS, and the Chinese Academy of Sciences (CAS) and the University of Wuhan (WHU) also became new contributors. The IGS GIM also contains satellites and receivers DCB values used in the solution (Hernández-Pajares et al. 2009; Roma-Dollase et al 2018; IGS 2020).

The GIM used in this research was produced by CODE, considering their temporal resolution is 1 h, i.e., half of the IGS GIM. Therefore, these are more suitable for Brazil due to the high temporal TEC variation. In such a solution, the VTEC is modeled on a geomagnetic solar reference system using a degree and order of 15 for the spherical harmonic expansion (Schaer 1999).

The topic of the modeling and estimation of the Regional Ionosphere Maps has been the target of investigations by the international and national scientific community in the last years (Camargo 1999; Opperman et al. 2007; Brunini et al. 2008; Zahra, Michael and Dave 2010; Aguiar and Camargo 2012; Aa et al. 2015; Zhao, Mekik and Feng 2016). To estimate the RIM, the data from a denser GNSS network for the region is used, which allows the production of ionosphere maps with better spatial and temporal resolutions than the GIM.

The MAGGIA started the production of the new RIM with coverage for Latin America at the end of 2018. The MAGN-RIM is estimated in near real-time using multi-frequency and multi-constellation data from GPS, GLONASS, Galileo and Beidou satellites. Furthermore, observations from more than two hundred GNSS stations located mainly in South America, but also Central America, North America, Europe, Africa and Antarctica are used as input to the MAGN-RIM estimation. The GNSS data is acquired in real-time via NTRIP allowing the production of RIM with a latency lower than 10 minutes (Mendoza, Meza and Aragón Paz 2019a).

The covered area of the MAGN-RIM is between 80° S and 40° N in latitude and 110° W and 0° E in longitude. The temporal resolution is fifteen minutes with a grid spacing of 0.5 degrees for the latitude and longitude, encompassing Central and South America, the Caribbean and the Antarctic Peninsula (Mendoza, Meza and Aragón Paz 2019a). Figure 2 shows a graphical representation of the MAGN ionospheric grid for march 17 of 2015 at 18 h (UTC) and Table 1 shows the main characteristics of the CODE-GIM and MAGN-RIM.



Source: Mendoza, Meza and Aragón Paz (2019a).

Figure 2: MAGN regional ionosphere map coverage.

Table 1: CODE-GIM and MAGN-RIM main characteristics.

Feature	CODE'S GIM	MAGN
Spatial resolution	2.5° x 5° (Lat and Long)	0.5° x 0.5° (Lat and Long)
Temporal Resolution	1 h	15 min
Latency	14 Days	few minutes
GNSS Network	IGS	SIRGAS-CON+
GNSS System	GPS	GPS+GLONASS+Galileo+BDS
DCB	Available	Not Available

Source: the authors.

From Fig 2 we can see that the MAGN grid is not continuous what occurs due to a lack of GNSS data in some areas. For the production of the MAGN maps, a data quality control procedure per station is carried out aiming to remove gross errors, where the observations resulting from the Melbourne-Wübbena (MW) linear combination, with outliers, cycle slips, and any receiver clock inconsistency are identified and discarded. The MW and ionosphere-free (IF) linear combinations, within each phase-continuous interval, are formed and modeled with a low-order polynomial. The resulting data intervals are evaluated and data with RMS greater than 0.6 cycles (MW) and 2.4 cycles (IF) are identified and rejected. At the end of the process, less than 7% of the observations are discarded, including those with elevation angle below 10° (Mendoza, Meza and Aragón Paz 2019b; Mendoza personal communication).

The VTEC in the MAGN-RIM is modeled based on a fixed Sun frame using Green's function and the mapping function used is the Modified Single Layer Model (MSLM) (Mendoza, Meza and Aragón Paz 2019b).

Until December 13 of 2019, the receiver and satellites DCBs were computed as daily constants values, and after that, the DCB started to be estimated as constant plus a linear trend with two update rates, once a day and every 15 minutes (Mendoza, Meza and Aragón Paz 2019b). The next section shows the material and methods used in our analysis.

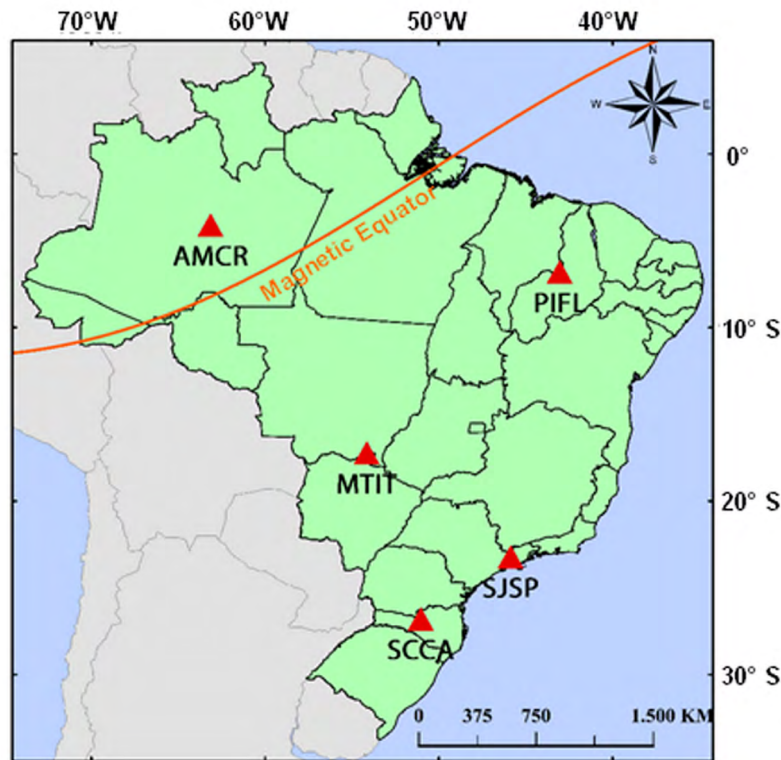
3. Material and methods

To assess the performance of MAGN-RIM, the GPS data collected on five reference stations in Brazil were processed. The single-frequency positioning was applied to evaluate the accuracy improvement using the MAGN-RIM and CODE-GIM where the solution from IF combination was used as a baseline for comparison. This section describes the dataset, the software, and the data processing strategy used, as well as how the results were analyzed.

3.1 Data

The performance of the MAGN-RIM was analyzed considering GPS data from five RBMC stations (see Figure 3) located at different geomagnetic latitudes (SCCA: -21.175° , SJSP: -21.759° , MTIT: -12.199° , PIFL: -10.004° and AMCR: 3.682°). The MAGN-RIM analyzed refers to the first year of the available data, i.e., the year 2019, which is under a low solar activity period. We developed scripts to automatically download the RINEX files as well as the CODE and MAGN maps, respectively, from IBGE, IGS, and MAGGIA FTP servers.

Due to the direct relationship between solar activity and geomagnetic conditions with GNSS positioning quality, the behavior of the solar flux at 10.7 cm (2800 MHz) and Dst (Disturbance Storm Time) indexes were analyzed during the period of the experiment. As stated by Fejer et al. (1991) the solar activity can be classified as: low, $F_{10.7} < 100$; moderated, $100 \leq F_{10.7} \leq 150$; and high, $F_{10.7} > 150$. A classification on the geomagnetic conditions based on Dst index was proposed by Loewe and Prölss (1997) as: weak, -50 nT to -30 nT; moderated, -100 nT to -50 nT; strong, -200 nT to -100 nT; severe, -350 nT to -200 nT; and great, < -350 nT. The maximum $F_{10.7}$ and minimum Dst observed were 81.8 sfu and -65 nT, respectively. Thus, it can be stated that 2019 was a period of low solar activity and weak to moderate variations in the geomagnetic field. Therefore, the experiment was carried out in a stable period of both solar activity and magnetic conditions that certainly will not critically affect the positioning results.



Source: the authors.

Figure 3: Location of RBMC stations used in the experiments.

3.2 Precise Absolute Positioning

GPS data processing was performed using the in-house RT-PPP which is capable of computing the absolute GPS positioning in static and kinematic mode taking into account mathematical models to correct several systematic effects affecting the GNSS observables (Marques 2012; Marques et al. 2014).

The GPS data for five stations were processed by applying double-frequency data derived from codes C1 and P2 to form the pseudorange IF combination, and also the single-frequency solution using only the C1 code with ionosphere correction from GIM and RIM. When the P2 code is not available we try to use the C2 code. The satellites DCBs P1-C1 and P2-C2 were applied to the observations for the compatibilization of the C1 and C2, respectively, with P1 and P2, that is the same observables are used to generate the IGS products. The absolute positioning was accomplished in the static case within a daily base solution with a 10° elevation cut-off and the precision values of 0.8 m and 1 m were adopted, respectively for P1 and P2 observations.

The tropospheric delay was estimated using a stochastic random walk process and geodynamics effects such as tectonic plate motion, solid earth tides, and ocean tide loading are also modeled by the RT-PPP software. Although an offline RT-PPP version was used in this investigation, an online version is available at <<http://is-cigala-calibra.fct.unesp.br/ppp/index.php>>. Table 2 shows the main strategies implemented in the RT-PPP software.

Table 2: Systematic effects modeling options on RT-PPP.

Effect	Strategy
Ionosphere – 1st order	<i>Ion-free</i>
	Stochastic process
Troposphere	Ionosphere maps
	Hopfield + GPT
	GMF + ZTD from CPTC
	VMF1 + ZTD from ECMWF
PVC (receiver and satellite)	ZHD constrained + ZWD estimated (<i>Random Walk</i>)
Precise Ephemeris	Absolute antenna Phase Center Corrections (PCO e PCV)
Satellite clock error	From IGS
Differential Code Bias	Estimated
Ambiguities	Monthly solutions from CODE
	Float solution

Source: Adapted from Marques (2012).

3.3 MAGN RIM assessment

To analyze the MAGN-RIM performance we processed GPS data in the absolute positioning by using ionosphere corrections from MAGN-RIM and CODE-GIM. Both solutions were compared with the ionosphere-free solution that was assumed as ground-truth. Then, we obtained the differences of the coordinates from MAGN-RIM and CODE-GIM solutions with the ionosphere-free solution. Therefore, we will denominate such differences as MAGN-RIM and CODE-GIM “errors”. In such a case, the geodynamic effects are canceled out and do not affect the analysis.

The coordinate differences or “errors” were evaluated in a local geodetic coordinate system allowing the analysis of the altimetric (Up) and planimetric components (E and N) independently. The Up component is most affected by the non-modeled ionospheric delay (Choy, Zhang and Silcock 2008). Therefore, the computed coordinate differences are denominated hereinafter as DE, DN and DU.

The errors computed from MAGN-RIM and CODE-GIM versus IF are analyzed for each GNSS station and the statistics used were the maximum absolute, mean, standard deviation and RMS error (RMSE).

Considering there are some incomplete MAGN maps throughout the year 2019, and atypical behavior of MAGN solution between the days 260 and 344 of 2019, the statistics were calculated taking the following cases into account:

- I - all data processed;
- II – exclusion of the period between days 260 and 344, and
- III – case II plus exclusion of the days when the MAGN maps were incomplete.

Incomplete MAGN maps appear due to problems occurring in real-time communication. Besides that, the analyses of the solar activity and geomagnetic indexes indicate no irregularities in the ionosphere during days 260 and 344, and no changes could be observed in the adopted procedures to estimate the MAGN-RIM. Therefore, such a situation requires further investigation.

To carry out a global analysis on the performance of MAGN-RIM when compared to CODE-GIM solution, a relative performance (Ω) indicator was computed, according to the following equation:

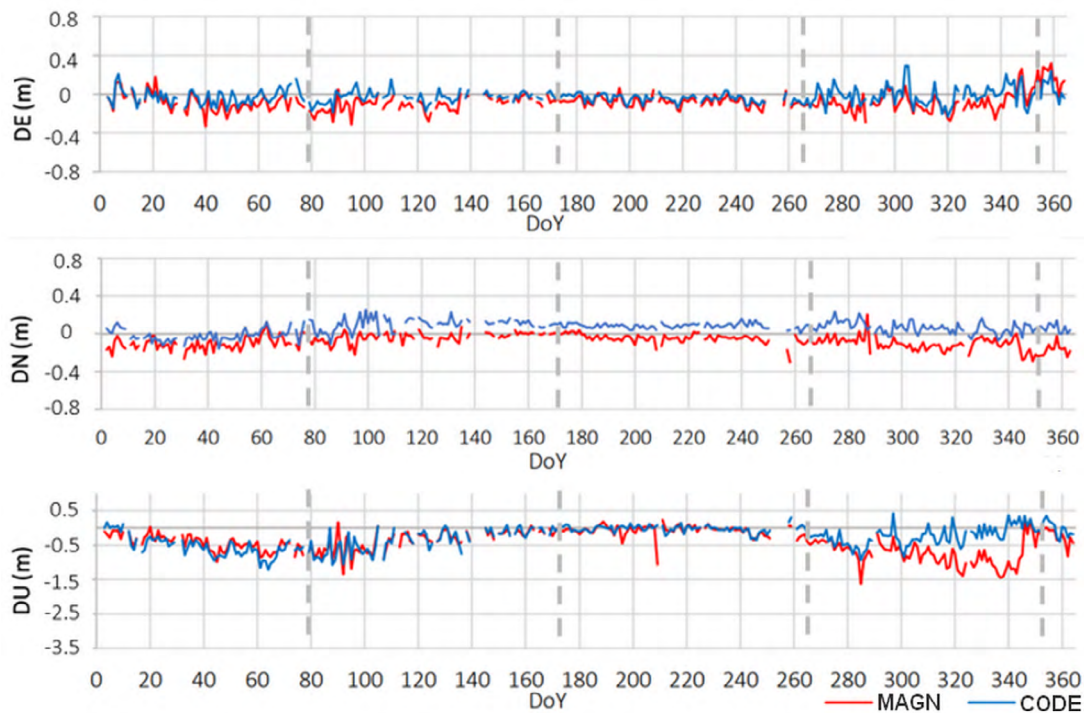
$$\Omega = 100 - \left(\frac{RMSE_{MAGN}}{RMSE_{CODE}} \right) 100 \quad (5)$$

where $RMSE_{MAGN}$ and $RMSE_{CODE}$ are computed for each component (DE, DN, DU) obtained respectively, by the MAGN-RIM and CODE-GIM solutions in comparison with the IF solution. The relative performance was computed for each station as well as considering all stations. In the latter case, the relative performance is called Ω_{Br} .

4. Results and discussions

Figures 4 to 8 show the time series of the differences between the reference coordinates (IF solution) and those estimated in the absolute positioning by using the CODE-GIM (in blue) and MAGN-RIM (in red). The south hemisphere autumn and spring equinoxes (days 79 and 266 of 2019), as well as winter and summer solstices (days 172 and 355 of 2019), are represented by vertical dashed lines. The y-axis scales are slightly different for the planimetric and altimetric components to facilitate the visualization.

Figure 4 shows the differences in the coordinates found for the SCCA station.



Source: the authors.

Figure 4: Coordinates differences (MAGN and CODE versus IF solutions) at SCCA.

From figure 4 we can see that the performance is similar for both ionosphere maps providing more accurate positioning for the planimetric components (DE and DN) what is expected considering the ionospheric errors affect mainly the altimetric component (Choy, Zhang and Silcock 2008). It is possible to observe peaks on days 208 and 284 of 2019 that occurred due to the use of incomplete MAGN maps in the data processing.

The biggest values for DU component start near the autumn and spring equinoxes and decrease in the winter solstice what can be related to the difficulties to model the ionosphere near the equatorial ionization

anomaly or Appleton anomaly.

We can also observe in the times series of Figure 4 the atypical behavior between the days 260 until 344 of 2019 for the MAGN-RIM solution. For such a period the CODE-GIM solution performed quite better than MAGN-RIM.

Table 3 shows the statistics for the two solutions (MAGN-RIM and CODE-GIM) considering the three cases described in section 3.3.

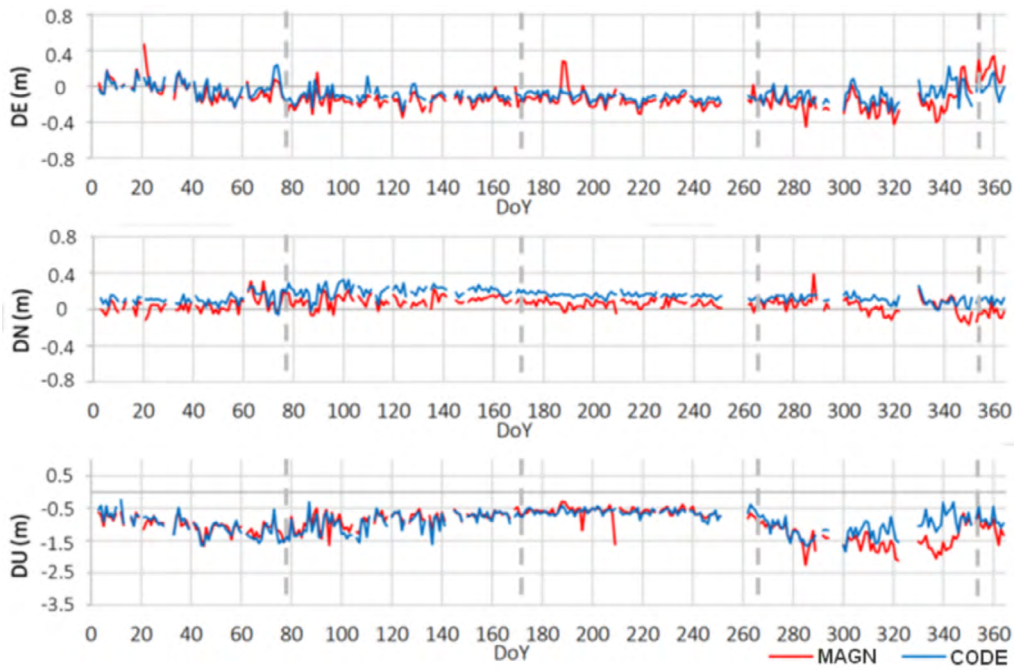
Table 3: SCCA statistics.

SCCA		DE (m)		DN (m)		DU (m)	
		CODE	MAGN	CODE	MAGN	CODE	MAGN
Mean	I	-0.025	-0.800	0.062	-0.076	-0.267	-0.399
	II	-0.028	-0.071	0.061	-0.070	-0.273	-0.278
	III	-0.027	-0.068	0.063	-0.069	-0.270	-0.270
Maximum Absolute	I	0.293	0.333	0.256	0.303	1.221	1,625
	II	0.237	0.333	0.256	0.303	1.221	1.341
	III	0.237	0.316	0.256	0.303	1.221	1.053
Std. Dev.	I	0.078	0.093	0.070	0.073	0.323	0.365
	II	0.069	0.096	0.073	0.075	0.338	0.285
	III	0.070	0.097	0.072	0.073	0.335	0.270
RMSE	I	0.082	0.123	0.093	0.106	0.419	0.542
	II	0.075	0.120	0.095	0.103	0.435	0.398
	III	0.075	0.118	0.096	0.101	0.430	0.382

Source: the authors.

From Table 3 we can confirm that the atypical behavior at the end of the year 2019 caused degradation in the MAGN-RIM solution. Therefore, removing from the analysis such period of data or the periods with missing maps (cases II and II) the Up component from MAGN-RIM presented a better RMSE value than the CODE-GIM solution.

Figure 5 shows the time series of errors for the MAGN-RIM and CODE-GIM solutions for the SJSP station, which is located in the crest region of the equatorial ionization anomaly. The average of the planimetric errors for the MAGN-RIM solution is near zero with the greatest values for DU, where the maximum values occur closest to the autumn and spring equinoxes. It is also possible to observe the degradation of the MAGN-RIM solution between days 260 and 344 of 2019.



Source: the authors.

Figure 5: Coordinates differences (MAGN and CODE versus IF solutions) at SJSP.

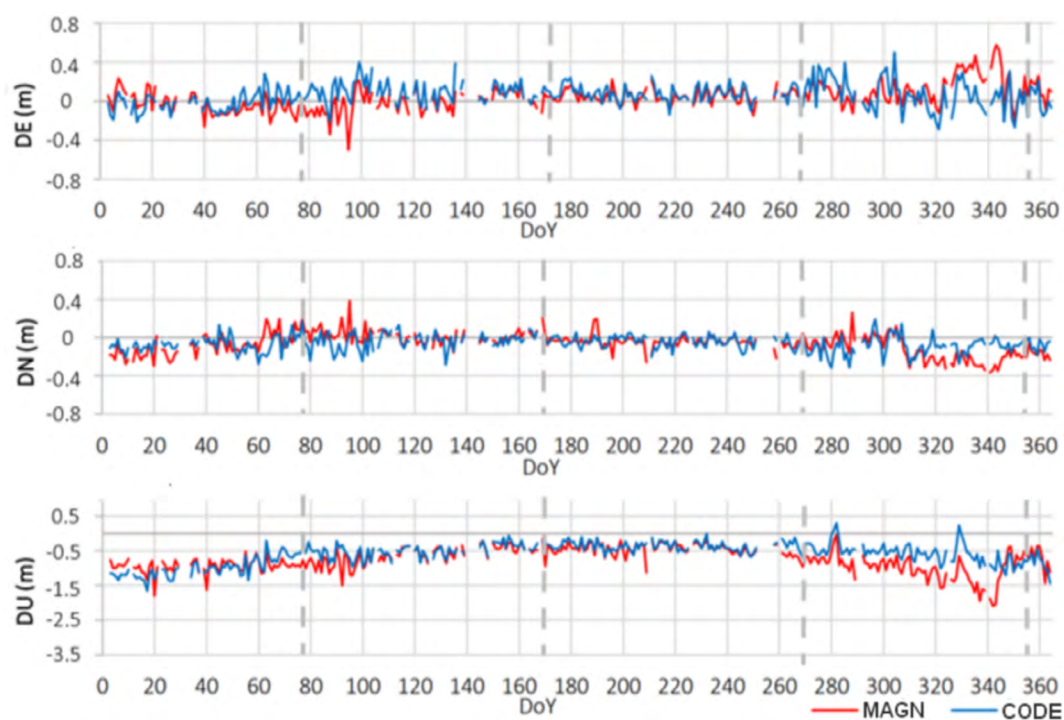
The SJSP statistics are presented in Table 4 and similar to what happened for SCCA station when removing the atypical period and missing maps (cases II and III) the MAGN-RIM solution presented better RMSE in the Up component than CODE-GIM. The same behavior can be observed for all stations taking part in the processing.

Table 4: SJSP statistics.

SJSP		DE (m)		DN (m)		DU (m)	
		CODE	MAGN	CODE	MAGN	CODE	MAGN
Mean	I	-0.085	-0.125	0.146	0.057	-0.907	-0.979
	II	-0.080	-0.103	0.155	0.057	-0.851	-0.834
	III	-0.078	-0.100	0.155	0.057	-0.855	-0.833
Maximum Absolute	I	0.293	0.466	0.325	0.384	1.844	2.254
	II	0.281	0.466	0.325	0.308	1.645	1.665
	III	0.281	0.466	0.325	0.308	1.645	1.665
Std. Dev.	I	0.089	0.128	0.064	0.075	0.328	0.405
	II	0.087	0.128	0.064	0.075	0.302	0.288
	III	0.088	0.129	0.065	0.075	0.304	0.279
RMSE	I	0.123	0.179	0.159	0.094	0.966	1.060
	II	0.119	0.164	0.168	0.094	0.905	0.884
	III	0.118	0.163	0.168	0.094	0.908	0.878

Source: the authors.

Figure 6 shows the time series of errors for MAGN-RIM and CODE-GIM in the MTIT station.



Source: the authors.

Figure 6: Coordinates differences (MAGN and CODE versus IF solutions) at MTIT.

Table 5 shows the statistics for the MTIT station where we can observe similar results to the stations SCCA (Table 3) and SJSP (Table 4).

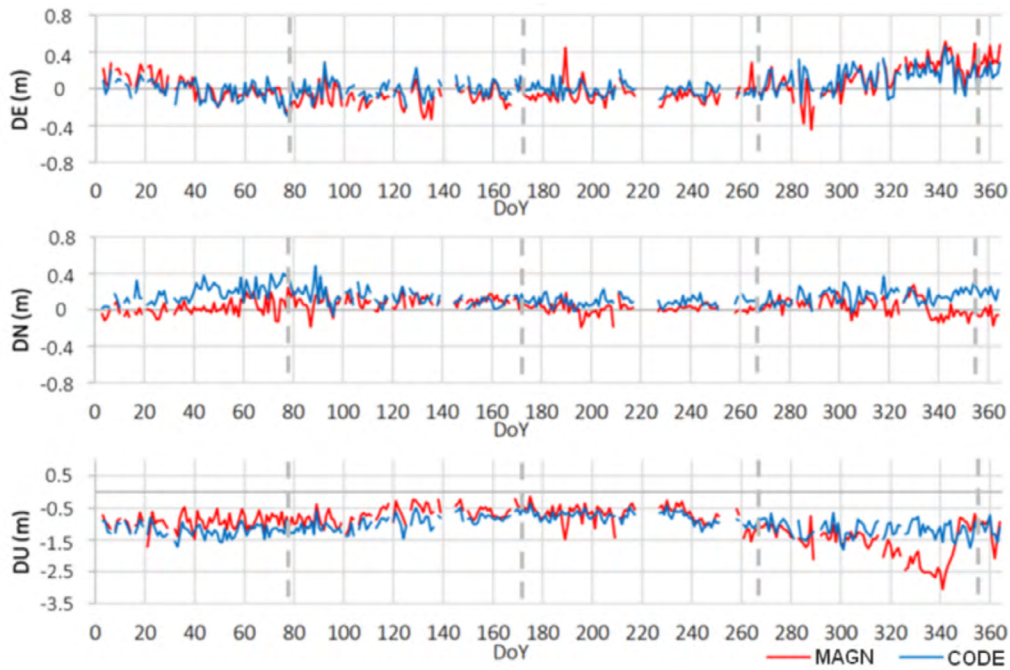
Table 5: MTIT Statistics.

MTIT		DE (m)		DN (m)		DU (m)	
		CODE	MAGN	CODE	MAGN	CODE	MAGN
Mean	I	0.056	0.037	-0.061	-0.066	-0.590	-0.739
	II	0.050	0.008	-0.052	-0.048	-0.617	-0.655
	III	0.051	0.012	-0.051	-0.049	-0.612	-0.635
Maximum Absolute	I	0.500	0.573	0.317	0.382	1.652	2.087
	II	0.397	0.499	0.286	0.382	1.652	1.787
	III	0.397	0.388	0.286	0.277	1.652	1.337
Std. Dev.	I	0.128	0.134	0.086	0.115	0.323	0.355
	II	0.116	0.113	0.078	0.102	0.336	0.299
	III	0.114	0.108	0.078	0.096	0.330	0.270
RMSE	I	0.140	0.139	0.105	0.133	0.673	0.821
	II	0.126	0.113	0.094	0.112	0.703	0.721
	III	0.125	0.108	0.093	0.108	0.696	0.691

Source: the authors.

Figure 7 shows the error time series of MAGN-RIM and CODE-GIM solutions for the PIFL station. A data gap due to GNSS receiver problems between days 218 and 224 of 2019 can be observed. Besides it was the most

affected by the atypical behavior in the MAGN-RIM solution, reaching an altimetric error of the order of 3 m. Table 6 shows the statistics for the PIFL station.



Source: the authors.

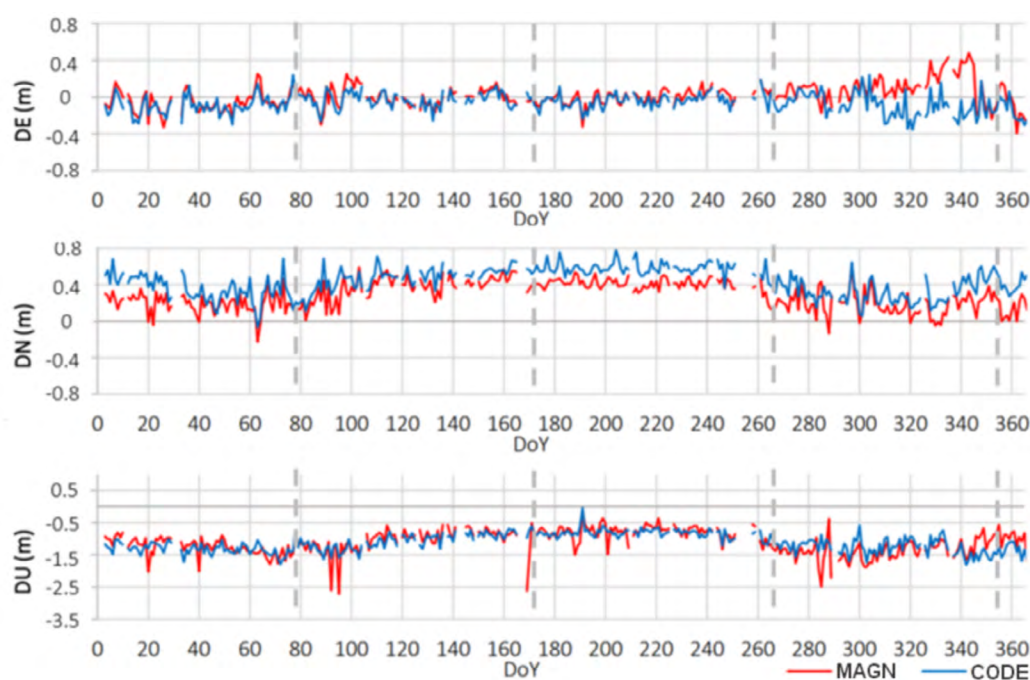
Figure 7: Coordinates differences (MAGN and CODE versus IF solutions) at PIFL.

Table 6: PIFL Statistics.

PIFL		DE (m)		DN (m)		DU (m)	
		CODE	MAGN	CODE	MAGN	CODE	MAGN
Mean	I	0.027	0.007	0.141	0.041	-1.033	-1.007
	II	0.002	-0.022	0.143	0.038	-0.995	-0.799
	III	0.001	-0.024	0.146	0.039	-0.997	-0.794
Maximum Absolute	I	0.461	0.512	0.482	0.275	1.805	3.045
	II	0.351	0.495	0.482	0.245	1.761	2.073
	III	0.351	0.495	0.482	0.245	1.761	1.986
Std. Dev.	I	0.119	0.162	0.087	0.083	0.276	0.519
	II	0.101	0.146	0.090	0.080	0.278	0.307
	III	0.100	0.148	0.089	0.078	0.275	0.295
RMSE	I	0.122	0.162	0.166	0.093	1.070	1.134
	II	0.102	0.148	0.169	0.089	1.035	0.858
	III	0.100	0.149	0.171	0.087	1.036	0.847

Source: the authors.

Figure 8 shows the error time series for the MAGN-RIM and CODE-GIM solutions in the AMCR station. The AMCR is also near the geomagnetic equator but from the side of the northern hemisphere. Table 7 shows the statistics computed for AMCR station.



Source: the authors.

Figure 8: Coordinates differences (MAGN and CODE versus IF solutions) at AMCR.

Table 7: AMCR Statistics.

AMCR		DE (m)		DN (m)		DU (m)	
		CODE	MAGN	CODE	MAGN	CODE	MAGN
Mean	I	-0.064	0.013	0.438	0.288	-1.119	-1.111
	II	-0.060	-0.022	0.475	0.320	-1.089	-1.019
	III	-0.058	-0.020	0.473	0.324	-1.089	-0.994
Maximum Absolute	I	0.355	0.481	0.781	0.618	1.812	2.714
	II	0.306	0.393	0.781	0.592	1.786	2.714
	III	0.306	0.354	0.781	0.592	1.786	2.619
Std. Dev.	I	0.106	0.131	0.155	0.152	0.284	0.381
	II	0.096	0.109	0.144	0.144	0.289	0.356
	III	0.096	0.107	0.144	0.141	0.287	0.313
RMSE	I	0.124	0.132	0.465	0.326	1.156	1.176
	II	0.113	0.101	0.497	0.351	1.129	1.081
	III	0.112	0.108	0.495	0.354	1.127	1.042

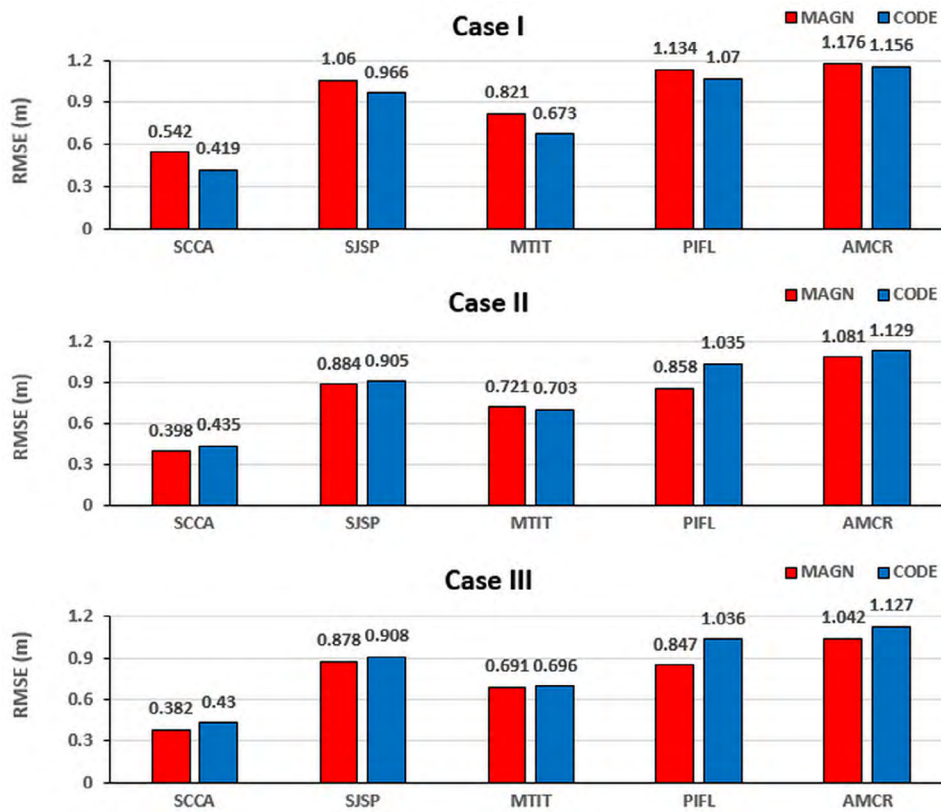
Source: the authors.

From Figure 8 several peaks can be observed in the error time series for the MAGN-RIM solution in the AMCR station. Such peaks occur due to missing data in the MAGN maps on days 21, 39, 91, 94, 169, 187, 200, 284, 287 and 288 of the year 2019. On the other hand, the MAGN-RIM solution for the AMCR was less affected by the atypical behavior among all stations.

From Figures 4, 5, 6, 7 and 8, we can see that the absolute positioning presented the worst results in the autumn and spring equinoxes for the stations SCCA, SJSP, AMCR and PIFL what can be related to difficulties in the

modeling of the equatorial ionization anomaly. For the MTIT station, the worst results in the absolute positioning occur near the summer solstice. It is also observed that the best positioning results applying both ionosphere maps (MAGN-RIM and CODE-GIM) were reached during the winter solstice for all stations considering that refers to a period with the lowest photoionization production.

The values of RMSE in the DU component for each station and cases are shown in Figure 9.



Source: the authors.

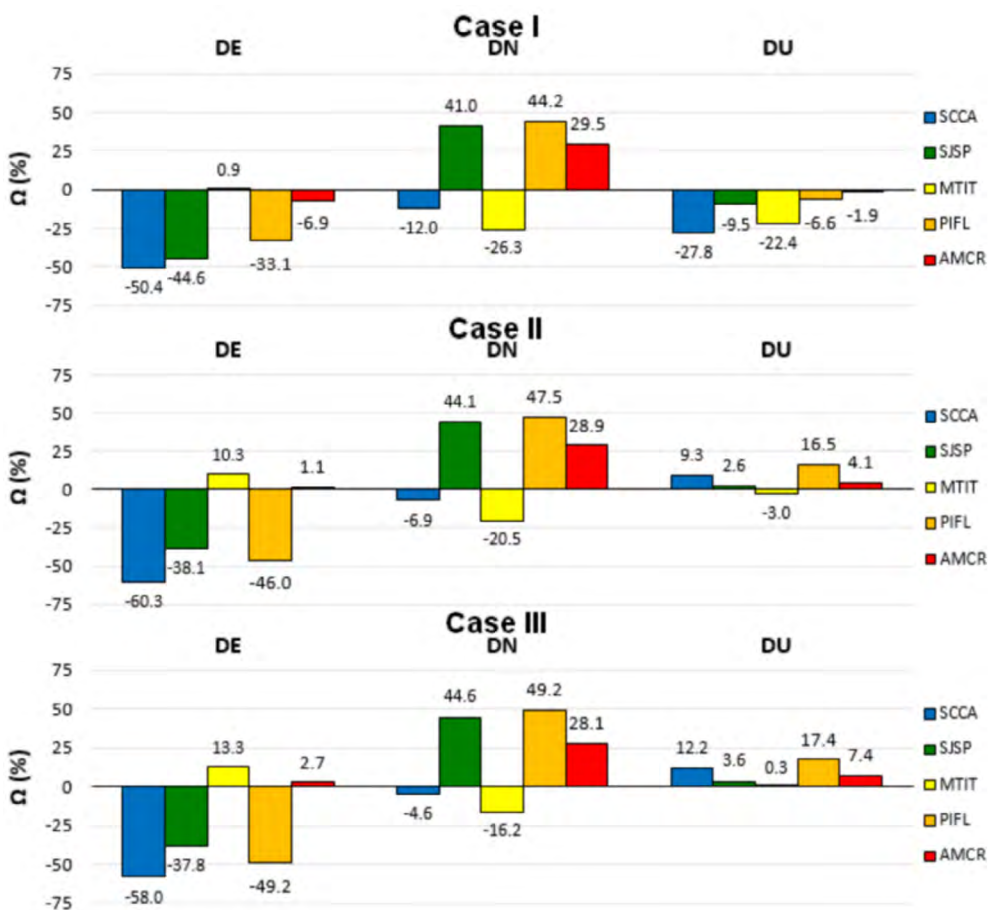
Figure 9: DU RMSE error for all stations and cases.

The worst DU RMSE for both MAGN and CODE solutions occurred for stations closest to the geomagnetic equator (AMCR and PIFL), followed by SJSP located near the equatorial anomaly crest, MTIT, and finally SCCA. From Figure 9, we can see that taking out the results with atypical behavior and with missing data in the MAGN maps, i.e., the case III, the DU RMSEs are better for all stations with GPS data processed in the absolute positioning and applying the MAGN-RIM.

Figure 10 shows the station’s relative performance provided by the MAGN-RIM solution concerning CODE-GIM for the 3 considered cases. Negative values represent worse performance for the MAGN solution. It can be observed that MAGN performance was 1.9% to 27.8% worse for the SCCA and AMCR stations, respectively, when all solutions were considered in the analysis.

On the other hand, after removing the anomalous period at the end of the year 2019 as well as the days with incomplete MAGN maps, the MAGN-RIM solution shows better results than CODE-GIM in the DU component for all stations, reaching improvements from the minimum of 0.3% to the maximum of 17.4% for the MTIT and PIFL, respectively.

In general, we can observe that MAGN-RIM solution provided better results for stations closest to the geomagnetic equator and the crest of the equatorial ionization anomaly, while the CODE-GIM solution presents better performance for the remaining of the stations.

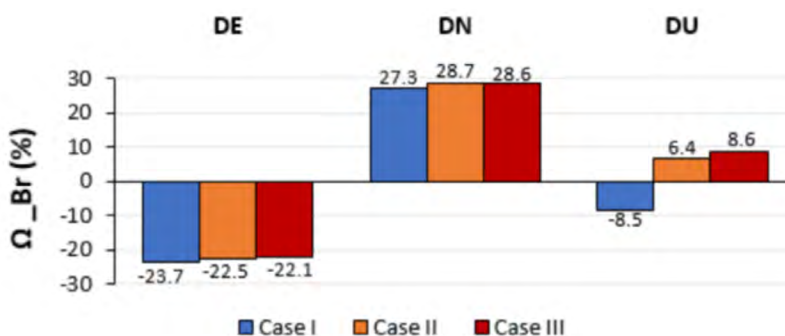


Source: the authors.

Figure 10: MAGN relative performance over CODE.

Figure 11 shows the overall relative performance of MAGN-RIM since it covers the results of the five stations.

The relative performance of the planimetric coordinates remains unchanged in the three cases, with MAGN achieving better results in the north and worse results in the east components. It also should be noted that in cases II and III the MAGN solution performed better than CODE in the up component.



Source: the authors.

Figure 11: Overall MAGN relative performance over CODE.

5. Concluding remarks

A performance assessment of the near real-time Regional Ionospheric Maps produced by the Universidad de La Plata in the single-frequency GNSS absolute positioning in Brazil during its first year of production was carried out in this paper. The absolute positioning results obtained with the new regional ionosphere maps were compared with those using the GIM produced by CODE, assuming as the ground truth the PPP solution with the ionosphere-free combination.

Atypical behavior was observed for the MAGN-RIM solution in some periods, which requires further investigations. When the abnormal periods are removed, there are considerable improvements for the Up component in the MAGN-RIM about the CODE-GIM solution.

Therefore, we can conclude that MAGN ionosphere maps can be considered a good option for modeling the first-order ionospheric effect in the absolute positioning in Brazil. Although some missing data and problems in the MAGN maps have been found, they present as the main advantage the lower latency than CODE's final GIM what makes it possible to process single-frequency GNSS data either in a post-processed mode or near real-time.

Finally, because the production of MAGN ionosphere maps started in late 2018, the experiments were carried out with data observed in a period of low solar activity. Therefore, as soon as the MAGN ionosphere maps are available in a period of higher solar activity, further analysis should be performed.

ACKNOWLEDGMENT

We would like to thanks IGS, CODE, IBGE, and especially, MAGGIA for providing the data used in this research. We also would like to thanks CNPq for supporting the first author through scholarship (Process 02/2019 PIBIC CNPq/UFU) as well as the valuable contribution of the reviewers and editor.

AUTHOR'S CONTRIBUTION

All three authors were responsible for the methodology, the analyzes, and the manuscript writing. Individually, Thiago Amaral Pereira was responsible for data acquisition and processing as well as for initial analysis; Wagner Carrupt Machado was the research proponent and has done deeper results analysis, and Haroldo Antonio Marques has also done deeper analysis and provided the GNSS data processing software.

REFERENCES

- Aa, E. Huang, W. Yu, S. Liu, S. Shi, L. Gong, J. Chen, Y. Shen, H. 2015. A regional ionospheric TEC mapping technique over China and adjacent areas on the basis of data assimilation. *J. Geophys. Res.: Space Phys*, 120(6), pp. 5049–5061. <https://doi.org/10.1002/2015JA021140>
- Aguiar, C. R. Camargo, P. O. 2012. Resolução espacial da grade ionosférica e do GIVE. *Boletim de Ciências Geodésicas*, 18(3), pp. 464-479. <https://doi.org/10.1590/S1982-21702012000300007>
- Aguiar, C. R. E. Kozelinski, A. 2015. Mapas de TEC IONEX em tempo real gerados pelo modelo GIB (Grade Ionosférica Brasileira). *Revista Brasileira de Cartografia*, 67(8), pp. 1569-1565.

- Armendaris, O. C. Matsuoka, M. T. Camargo P. O. 2009. Desempenho do modelo global da ionosfera do IGS: avaliação no posicionamento por ponto na região sul do Brasil em período de alta atividade solar. *Boletim de Ciências Geodésicas*, 15(2), pp. 208-223.
- Brunini, C.A. Meza, A. Gende, M. Azpilicueta, F. 2008. South American regional ionospheric maps computed by GESA: a pilot service in the framework of SIRGAS. *Advances in Space Research*, 42(4), pp.737–744. <https://doi.org/10.1016/j.asr.2007.08.041>
- Camargo, P. O. 1999. *Modelo regional da ionosfera para uso em posicionamento com receptores GPS de uma frequência*. PhD. Federal University of Paraná.
- Choy S., Zhang K., and Silcock. D. 2008. An Evaluation of Various Ionospheric Error Mitigation Methods used in Single Frequency PPP. *Journal of Global Positioning Systems*, 7(1). pp. 62-71.
- European Commission. 2016. *European GNSS (Galileo) Open Service Ionospheric Correction Algorithm for Galileo Single Frequency Users* [online] Available at: <https://www.gsc-europa.eu/sites/default/files/sites/all/files/Galileo_Ionospheric_Model.pdf> [Accessed 3 November 2020].
- Fejer, B. G., de Paula, E. R., González, S. A., Woodman, R. F. 1991. Average vertical and zonal F region plasma drifts over Jicamarca. *Journal of Geophysical Research*, 96(A8), pp. 13.901-13.906. <https://doi.org/10.1029/91JA01171>
- Hernández-Pajares. M. Juan, J. M. Sanz, J. Orus, R. Garcia-Rigo, A. Feltens, J. Komjathy, A. Schaer, S. C. Kraskowski, A. 2009. The IGS VTEC maps: a reliable source of ionospheric information since 1998. *Journal of Geodesy*, 83(3-4), pp. 263-275. <https://doi.org/10.1007/s00190-008-0266-1>
- Hofmann-Wellenhof, B., Lichtenegger, H., Wasle, E. 2018. *GNSS – Global Navigation Satellite Systems. GPS, GLONASS, Galileo, and more*. Springer New Yourk. 516 p.
- IGS. 2020. IGS products. [online] Available at: <<http://www.igs.org/products>>. [Accessed 3 November 2020].
- Klobuchar, J. A. 1987. Ionospheric time-delay algorithm for single-frequency GPS users. *IEEE Transactions on Aerospace and Electronic Systems*, 23(3), pp. 325-331. <https://doi.org/10.1109/TAES.1987.310829>
- Komjathy, A. 1997. *Global ionospheric total electron content mapping using global positioning system*. PhD. University of New Brunswick.
- Loewe, C. A.; Pröls, G. W. 1997. Classification and mean behavior of geomagnetic storms. *Journal of Geophysical Research*, 102(A7), pp. 14.209-14.213. <https://doi.org/10.1029/96JA04020>
- Marques, H. A. 2012. *PPP em tempo real com estimativa das correções dos relógios dos satélites no contexto de rede GNSS*. PhD. Universidade Estadual Paulista.
- Marques, H. A. Monico, J. F. G. Shimabukuro, M. Oyama R. T. Wentz, J. P. 2014. PPP em tempo real: fundamentos, implementação computacional e análises de resultados no modo estático e cinemático. *Revista Brasileira de Cartografia*, 66(6), pp. 1331-1345.
- Mendoza, L. P. O., Meza, A. M., and Aragón Paz, J. M. 2019a. A multi-GNSS, multi-frequency and near real-time ionospheric TEC monitoring system for South America. *Space Weather*, 17(5), pp. 654-661. <https://doi.org/10.1029/2019SW002187>
- Mendoza, L. P. O., Meza, A. M., Aragón Paz, J. M. 2019b. Technical note on the multi-GNSS, multi-frequency and near real-time ionospheric TEC monitoring system for South America. *EarthArxiv*, pp. 1-13. <https://doi.org/10.31223/osf.io/3vts6>
- Opperman, B. D. L. Cilliers, P. J. McKinnell, L. Haggard, R. 2007. Development of a regional GPS-based ionospheric TEC model for South Africa. *Advances in Space Research*, 39(5), pp. 808-815. <https://doi.org/10.1016/j.asr.2007.02.026>
- Radicella, S. M. 2009. The NeQuick model genesis, uses and evolution. *Annals of Geophysics*, 52(3-4), pp. 417-422. <https://doi.org/10.4401/ag-4597>

- Rocha, G. D. C. Marques, H. A. Monico, J. F. G. 2015. Acurácia do posicionamento absoluto GPS com correção da ionosfera advinda de mapas ionosféricos globais e regionais. *Boletim de Ciências Geodésicas*, 21(3), pp. 498-514. <https://doi.org/10.1590/S1982-21702015000300028>
- Roma-Dollase, D., Hernández-Pajares, M., Krankowski, A. Kotulak, K. Ghoddousi-Fard, R. Yuan, Y. Li, Z. Zhang, H. Shi, C. Wang, C. Feltens, J. Vergados, P. Komjathy, A. Schaer, S. García-Rigo, A. Gómez-Cama, J. M. 2018. Consistency of seven different GNSS global ionospheric mapping techniques during one solar cycle. *Journal of Geodesy*, 92, pp. 691–706. <https://doi.org/10.1007/s00190-017-1088-9>.
- Schaer, S. Gurtner, W. Feltens, J. 1998. Ionex: The ionosphere map exchange format version 1. In: *IGS Analysis Center Workshop*. Darmstadt, Germany, 9-11 February 1998.
- Schaer, S. 1999. Mapping and predicting the earth's ionosphere using the global positioning system. PhD. University of Berne.
- Setti Júnior, P. D. T. Alves, D. B. M. Silva, C. M. D. 2019. Klobuchar and Nequick G ionospheric models comparison for multi-GNSS single-frequency code point positioning in the brazilian region. *Boletim de Ciências Geodésicas*, 25(3): e2019016, pp. 1-16. <https://doi.org/10.1590/s1982-21702019000300016>
- Wang, Z., Xue, k., Wang, C., Zhang, T., Fan, I., Hu, Z., Shi, C., Jing, G. 2021. Near real-time modeling of global ionospheric vertical total electron content using hourly IGS data. *Chinese Journal of Aeronautics*, 34(2). pp. 386-395. <https://doi.org/10.1016/j.cja.2020.07.023>
- Zahra, B. Michael, T. Dave, N. 2010. Regional GPS-based ionospheric TEC model over Australia using Spherical Cap Harmonic Analysis. In: *38th COSPAR Scientific Assembly*. Bremen, Germany, July 2010.
- Zhao, X. J. S., Mekik, C., Feng, J. 2016. Evaluation of regional ionospheric grid model over China from dense GPS observations. *Geodesy and Geodynamics*, 7(5). pp. 361-368. <https://doi.org/10.1016/j.geog.2016.04.011>